SCIENCE CHINA

Technological Sciences



Article

March 2023 Vol.66 No.3: 869–880 https://doi.org/10.1007/s11431-022-2254-1

Multifunctional application of nonlinear metamaterial with two-dimensional bandgap

CHEN KangKang¹, TU GuoWei², DONG XingJian^{1*}, HUANGFU YiFan¹ & PENG ZhiKe^{1,3}

State Key Laboratory of Mechanical System and Vibration, Shanghai Jiao Tong University, Shanghai 200240, China;
 Department of Civil and Environmental Engineering, University of Michigan, Ann Arbor, MI 48109, USA;
 School of Mechanical Engineering, Ningxia University, Yinchuan 750021, China

Received August 4, 2022; accepted November 7, 2022; published online February 16, 2023

Mechanical metamaterials with low-frequency and broadband bandgaps have great potential for elastic wave control. Inspired by the ancient window mullions, a novel plate-type metamaterial with a two-dimensional bandgap is designed. Based on the local resonance mechanism, the broadband low-frequency in-plane and out-of-plane bandgaps on the designed structure are realized. The bandgaps can be adjusted by the mass re-distribution of the main-slave resonators, the stiffness design of the support beam, and the adjustment of the excitation amplitude. A semi-analytical method is proposed to calculate the in-plane and out-of-plane bandgaps and the corresponding wave attenuation characteristics of the infinite periodic metamaterial. We explored how mass redistribution, stiffness changes, and geometric nonlinearity influence the bandgap. Then, to verify the conclusions, we fabricated a finite periodic structure and obtained its wave transmission characteristics both numerically and experimentally. Finally, the designed metamaterial is applied to the waveguide control, elastic wave imaging, and vibration isolation. This study may provide new ideas for structural design and engineering applications of mechanical metamaterials.

mechanical metamaterial, two-dimensional bandgap, geometric nonlinearity, waveguide control, vibration isolation

Citation: Chen K K, Tu G W, Dong X J, et al. Multifunctional application of nonlinear metamaterial with two-dimensional bandgap. Sci China Tech Sci, 2023, 66: 869–880, https://doi.org/10.1007/s11431-022-2254-1

1 Introduction

Mechanical metamaterials have great potential in engineering fields [1,2], such as vibration isolation [3], energy storage [4–6], acoustic cloak [7,8], and compressive sensing [9,10]. There are still some challenges in the design of metamaterials. For practical application in a low-frequency environment, the bandgap and bandwidth of the metamaterial should be adjustable. More attention should be paid to the influence of geometric nonlinearity and multi-dimensional excitations on the transmission characteristics of elastic waves. With the improvement of manufacturing levels [11,12], engineering applications of metamaterials should be further explored. The research status will be reviewed from three aspects: The

In mechanical fields, a low-frequency, broadband bandgap has always been a target [13,14]. Regarding elastic waves, the bandgap is mainly formed by Bragg scattering, inertial amplification, and local resonance [3,15,16]. The Bragg scattering mechanism is limited by Bragg's law, that is, an ultra-low frequency bandgap requires an extremely large lattice constant, which is difficult to achieve in practice. The inertial amplification mechanism often needs external moving components to amplify the effective inertia of the small mass [17], which limits the application range of the principle. While using a locally resonant structure, we just need to lower the stiffness of the resonator to obtain a low-frequency bandgap [14,18–20]. As for broadband tunability of the

principle and control method of the low-frequency and broadband bandgap, the passive control of the bandgap of thin-walled structures, and the metamaterial application.

^{*}Corresponding author (email: donxij@sjtu.edu.cn)

bandgap, active [15,21], semi-active [22–25], and passive control [19,26] are some recently developed strategies. Gao and Wang [21] proposed an active metamaterial with feedback control. The metamaterial has tunable negative effective stiffness and tunable bandgap under symmetric feedback signals, while it can achieve nonreciprocal wave transmission over a broad frequency range under asymmetric feedback signals. Chen et al. [25] built a semi-active isolator with magnetorheological elastomer structures to control the vibration bandgap, and the vibration isolation performance is discussed under different frequencies and coil currents. The active control requires external devices such as actuators, sensors, and micro-controllers, to realize the real-time tuning of structural bandgaps [3]; the semi-active control also requires external equipment to adjust the bandgap, but it does not require internal feedback and real-time control systems. These bulky, costly attachments limit the use of active and semi-active control in real engineering. By contrast, passive control is a feasible strategy.

Thin-walled structures draw much attention to the passive control of bandgaps [27]. Some scholars achieved the passive control of the bandgap through changed mass [28–31], stiffness [29,30], preload [32–34], and so on. An et al. [29] realized the low-frequency bandgap of the planar metamaterial by using the thin beams as the support structure of the resonator and analyzed the influence of structural parameters on the bandgap properties. Li et al. [30] designed spiral beams with weak stiffness as the support structure of the resonator and the low-frequency bandgaps can be changed by the support stiffness and resonator mass. Inspired by biological materials, Zhang and Feng [32] designed a kind of soft metamaterial and its bandgap can be regulated in a wide frequency range through preloading. To obtain superior vibration reduction performance, Xiong et al. [35] optimize the structural parameters with the asymptotic optimization method to increase bandgap width. In the above research, the low-frequency bandgap is mostly achieved by the local resonance with a support structure of weak stiffness. However, the geometrical nonlinearity occurs inevitably in the support structure due to large deflection, which should not be ignored in the control of elastic waves [36,37]. Fang et al. [13] analyzed both theoretically and experimentally the influence of the nonlinear chaotic mechanism on the wave transmission characteristics in the one-dimensional and two-dimensional nonlinear metamaterial. Yu et al. [38] proposed the combinational design of the linear and nonlinear metamaterials and analyzed the influence of variable combination forms on wave suppression properties, which provides a novel idea for the nonlinear metamaterial. Besides, engineering structures are often subjected to multi-directional excitation. The designed structures should be capable of attenuating both in-plane and out-of-plane waves simultaneously [39]. Therefore, structures with two-dimensional

bandgaps should be taken seriously [15,40].

On top of metamaterial design, multi-functional applications are being explored. Utilizing the attenuation effect of the bandgap on waves, researchers [3,19,41–43] applied mechanical metamaterials to vibration isolation/suppression for beam, plate, and three-dimensional structures. Using the nonlinear coupling effect of multiple local resonances, Fang et al. [44] designed a nonlinear metamaterial to explore its vibration suppression and acoustic radiation in the low-frequency range. Zhao et al. [45] discussed the application of three-dimensional chiral metamaterials on bandgap control and vibration isolation, which may have potential in gradient design and digital coding. In terms of elastic wave control, some scholars have achieved directional waveguide transport [46–48]. Using the elastic valley Hall effect and the control system of magnetic fluid, Zhang et al [46] realized the waveguide control in elastic media. Chen et al. [49] studied the transmission characteristics of the transverse waveguide at the topological interface of the tunable membrane-type acoustic metamaterial. Another focus is energy absorption and harvesting in mechanical metamaterials [50,51]. Based on the mass-spring model, Lan et al. [50] analyzed both analytically and numerically the energy localization performance of locally resonant topological metamaterials and proved that the defect mode can enhance the energy harvesting performance. In addition, some scholars have achieved phononic diodes transmission [52], acoustic imaging [53,54], and microparticle manipulation [55,56]. There is still spacious room to explore the application of mechanical metamaterial.

Some existing structures are mainly applied to achieve a low-frequency bandgap through the local resonance principle with a flexible structure of weak stiffness. However, the geometric nonlinearity of the flexible structure is often ignored. Compared with the existing research, the semi-analytical method is proposed to consider the geometric nonlinearity of the flexible structure. The influence of nonlinear characteristics caused by the large deflection of the flexible structure on the bandgap is emphasized in this paper. Some existing structures only have a single-direction bandgap, which leads to certain limitations when subjected to multi-directional excitations. The designed structure intends to provide good design capability for two-dimensional bandgap through the mass arrangement of main-slave resonators, stiffness design of the supporting beam, and excitation amplitude. Compared with existing metamaterial applications, some applications of the designed structure, waveguide control, and elastic wave imaging, are explored further.

In this study, inspired by ancient window mullions, we designed a novel metamaterial plate for passive control of structural bandgap. The bandgap is changed through the reconfiguration of main-slave resonators and the adjustment of

the supporting beam. We analyzed the influences of nonlinearity of flexible beams under large deflection on bandgap. Finally, we adopt the designed structure to achieve the control of the waveguide path, the imaging of the phononic crystal plate, and the vibration isolation of a double-layered bolted plate. These applications will contribute to the advancement of mechanical metamaterials. This paper is organized as follows. Section 2 describes the design and the nonlinearity characteristics of the designed structure. The semi-analytical method and experiment are developed in Section 3. The parametric study is carried out in Section 4. The potential applications are illustrated in Section 5. Conclusions are drawn in the last section.

2 Design

Thin-walled structures are commonly used as connection or support structures in engineering equipment. For the thin plate, in addition to the in-plane excitation, it is inevitable to suffer the out-of-plane excitation (see Figure 1(a)). The ancient window mullions can ensure the stability of the wooden structure under the excitation of wind and dust from multidirections. Inspired by ancient window mullions, a phononic crystal with a local resonance mechanism for a two-dimensional and low-frequency bandgap is designed (see Figure 1(b)). The designed structure consists of three parts: The resonators, the curved beams, and the frame (see Figure 1(c)). The lattice constant is L_1 , which is less than the wavelength of the material (the frequency range of interest is below 800 Hz). The resonator comprises the main resonator and four slave resonators with radii R_1 and R_2 , respectively. The curved beam with thickness δ acts as a supporting structure to connect the resonator and the frame.

It should be noted that the geometric nonlinearity of the support beam with weak stiffness should be considered. Based on the local resonance mechanism, weak support stiffness of the resonator is required to achieve the low-frequency bandgap. However, geometric nonlinearity inevitably arises due to the large deformation of the curved beams. For the designed structure, the finite element method (see Appendix A) is employed to calculate the nonlinear

relation between the load and displacement of the curved beams under in-plane and out-of-plane motions, as shown in Figure 2. The curved beams under in-plane or out-of-plane loads appear obvious deformation (see Figure 2(a)). The displacements of the center under in-plane and out-of-plane are marked as u_j and w_j , respectively. The displacement of the resonator under different loads is shown in Figure 2(b), which shows the hardening nonlinearity of the curved beam. The nonlinear forces of the in-plane (F_x^{non}) and out-of-plane (F_z^{non}) can be fitted by finite-order polynomials. According to extensive testing, the relation between nonlinear force and the displacement under in-plane and out-of-plane can be expressed as

$$F_x^{\text{non}} = k_x u_j + p u_j^3, \tag{1}$$

$$F_z^{\text{non}} = k_z w_j + b w_j^3, \tag{2}$$

where k_x and k_z are the linear components of the nonlinear stiffness for the in-plane and out-of-plane motions, respectively. p and b are the coefficients that determine the degree of nonlinearity for the in-plane and out-of-plane motions, respectively.

3 Models and methods

Considering the geometric nonlinearity of the flexible beam under large deflection, a semi-analytical method is proposed to calculate the in-plane and out-of-plane dispersion relations. The experiment is set up to test the wave transmission characteristic of the designed structure.

3.1 Semi-analytical method

The in-plane motion of the designed structure is simplified (see Figure 3). The total mass of the main-slave resonators is taken as the local mass $m_{\rm r}$, and the flexible beam is simplified as a nonlinear spring with damping along the x-direction ($k_x^{\rm non}$ and c_x). The frame is regarded as the lumped mass M, and the adjacent frames are connected by the equivalent spring K_x . The equation of motion of the equivalent model can be expressed as

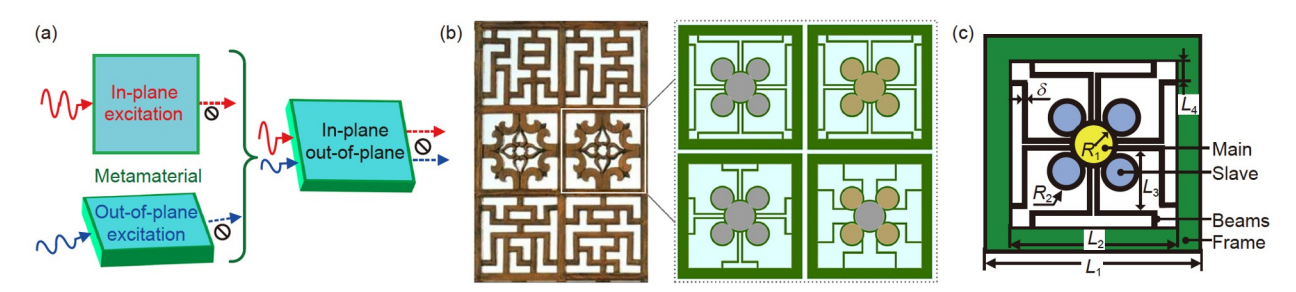


Figure 1 (Color online) Designed structure and geometrical parameter. (a) In-plane and out-of-plane excitations applied to plate structure; (b) ancient window mullion and the designed structure; (c) geometrical parameter.

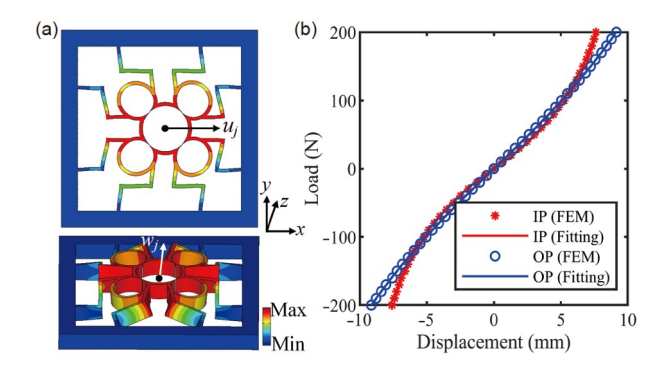


Figure 2 (Color online) Relationship between the displacement and load under large deflection. (a) Displacements under in-plane and out-of-plane; (b) nonlinear curves between load and displacement.

$$\begin{cases}
M_0 \frac{\mathrm{d}^2 x_j}{\mathrm{d}t^2} + K_x (2x_j - x_{j-1} - x_{j+1}) + m_r \frac{\mathrm{d}^2 u_j}{\mathrm{d}t^2} = 0, \\
m_r \frac{\mathrm{d}^2 u_j}{\mathrm{d}t^2} + c_x \frac{\mathrm{d}u_j}{\mathrm{d}t} + F_x^{\text{non}} + m_r \frac{\mathrm{d}^2 x_j}{\mathrm{d}t^2} = 0,
\end{cases}$$
(3)

where $M_0=M+m_r$, F_x^{non} is the nonlinear restoring force of the spring k_x^{non} , x_j and u_j denote the displacements of the *j*th lumped mass and the local mass, respectively.

To simplify the solving process, the dimensionless form of the equation of motion is obtained. First, the dimensionless restoring force can be obtained by dividing F_x^{non} by $k_x L_1$. The dimensionless form F_x^{non} can be expressed as

$$\overline{F}_{x}^{\text{non}} = \overline{u}_{j} + \frac{pL_{1}^{2}}{k_{-}} \overline{u}_{j}^{3} = \overline{u}_{j} + \eta L_{1}^{2} \overline{u}_{j}^{3}, \tag{4}$$

where $\overline{u}_j = u_j / L_1$, k_x is the linear component of the nonlinear spring k_x^{non} , η is the coefficient that determines the degree of nonlinearity, $\eta = p/k_x$. Furthermore, the dimensionless forms of eq. (3) can be written as

$$\begin{cases} \ddot{x}_{j} + \frac{1}{1+\alpha} (2x_{j} - x_{j-1} - x_{j+1}) + \frac{\alpha}{1+\alpha} \ddot{u}_{j} = 0, \\ \ddot{u}_{j} + \frac{2\zeta_{x}}{\alpha} \dot{u}_{j} + \mu L_{1} F_{x}^{\text{non}} + \ddot{x}_{j} = 0, \end{cases}$$
(5)

where \ddot{x}_j and \ddot{u}_j are the second derivatives of x_j and u_j with respect to τ , the normalized time $\tau = \omega_0 t$, ω_0 is the natural frequency of the lumped mass, $\omega_0 = \sqrt{K_x/M}$, the damping

ratio
$$\zeta_x = c_x / (2\sqrt{MK_x})$$
, $\alpha = m_x / M$, $\beta = k_x / K_x$, and $\mu = \beta / \alpha$.

The dispersion relation of the unit cell under linear undamped conditions is derived firstly, which has certain guidelines for the bandgap control of linear systems. Ignoring the damping and nonlinearity (ζ_x =0, p=0), the dynamic equation of the infinite periodic structures can be simplified as

$$\begin{cases} \ddot{x}_j + \frac{1}{1+\alpha} (2x_j - x_{j-1} - x_{j+1}) + \frac{\alpha}{1+\alpha} \ddot{u}_j = 0, \\ \ddot{u}_j + \mu u_j + \ddot{x}_j = 0. \end{cases}$$
 (6)

The solution of eq. (6) can be expressed in the form of a traveling wave solution [57,58]:

$$x_i = A_i e^{i(jqL_1 - \Omega\tau)}, \tag{7}$$

where $\Omega = \omega/\omega_0$, ω is the excitation frequency, A_j is the wave amplitude, q is the wave number. According to the Bloch theorem, the displacement of the adjacent lumped mass can be expressed as

$$x_{i-1} = e^{-iqL_1} \cdot x_i, \ x_{i+1} = e^{iqL_1} \cdot x_i.$$
 (8)

Substituting eqs. (7) and (8) into eq. (6), u_j can be calculated. The dispersion relation of the unit cell under linear undamped conditions can be calculated by

$$\cosh(qL_1) = 1 + \frac{\Omega^4 - (\mu + \beta)\Omega^2}{2(\mu - \Omega^2)}.$$
(9)

Furthermore, considering the damping and nonlinear stiffness of the resonators, the dispersion relation of the unit cell is derived by the harmonic balance method [59]. By inserting eq. (4) into eq. (5), the motion equations of the system are written as

$$\begin{cases} \ddot{x}_{j} + \frac{1}{1+\alpha} (2x_{j} - x_{j-1} - x_{j+1}) + \frac{\alpha}{1+\alpha} \ddot{u}_{j} = 0, \\ \ddot{u}_{j} + \frac{2\zeta_{x}}{\alpha} \dot{u}_{j} + \mu(u_{j} + \eta u_{j}^{3}) + \ddot{x}_{j} = 0. \end{cases}$$
(10)

To solve the motion equations, the time response of the *j*th resonator in complex Fourier series form [57] is assumed as

$$u_{j}(\tau) = \sum_{k=1}^{m} \varepsilon^{(k-1)/2} (A_{k,j} e^{ik\Omega\tau} + \overline{A}_{k,j} e^{-ik\Omega\tau}), (k=1, 3, ..., m),$$
(11)

where $A_{k,j}$ is the time-domain amplitude of the jth resonator

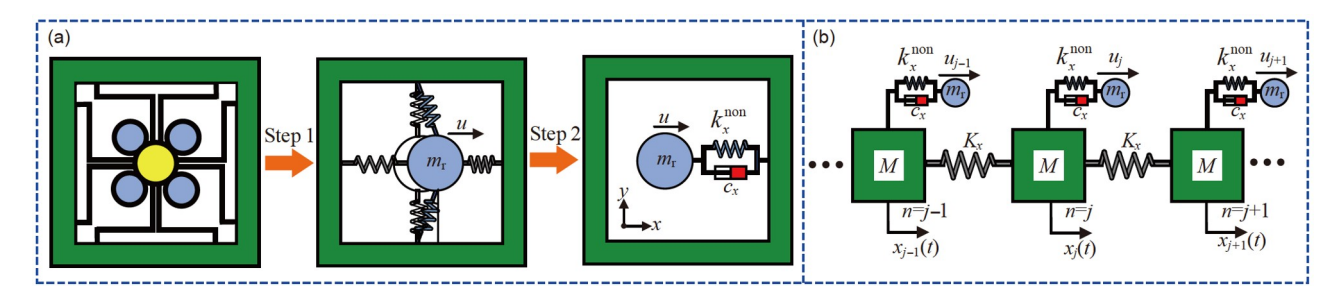


Figure 3 (Color online) Lumped mass-spring model for the in-plane motion. (a) Simplified process of the unit cell; (b) infinite periodic structure.

with k order, ε is a dimensionless parameter marking the order of the amplitude. Substituting eq. (11) into eq. (10) and integrating twice to τ , the displacement of the lumped mass can be expressed as

$$x_{j}(\tau) = \left(-A_{1,j} + \frac{\mu A_{1,j}}{\Omega^{2}} + \frac{2i\zeta_{x}A_{1,j}}{\alpha\Omega} + \frac{3\mu\eta A_{1,j}^{2}\overline{A}_{1,j}}{\Omega^{2}}\right)e^{i\Omega\tau} + \varepsilon \left(-A_{3,j} + \frac{2i\alpha}{3\zeta_{x}\Omega}A_{3,j} + \frac{\mu}{9\Omega^{2}}A_{3,j} + \frac{\mu\eta}{9\Omega^{2}}A_{1,j}^{3}\right)e^{i3\Omega\tau} + cc + O(\varepsilon^{2}),$$
(12)

where cc denotes the complex conjugate of the existing components; $O(\varepsilon^2)$ is the infinitesimal equivalence. The influences of high-order terms on system response are neglected here. By introducing the Bloch theorem, the displacement of the adjacent lumped mass can be calculated by

$$x_{j+1}(\tau) = \left(-A_{1,j} + \frac{\mu A_{1,j}}{\Omega^2} + \frac{2i\zeta_x A_{1,j}}{\alpha \Omega} + \frac{3\mu \eta A_{1,j}^2 \overline{A}_{1,j}}{\Omega^2} \right) e^{i\Omega \tau} e^{iqa} + cc,$$
(13)

$$x_{j-1}(\tau) = \left(-A_{1,j} + \frac{\mu A_{1,j}}{\Omega^2} + \frac{2i\zeta_x A_{1,j}}{\alpha \Omega} + \frac{3\mu \eta A_{1,j}^2 \overline{A}_{1,j}}{\Omega^2} \right) e^{i\Omega \tau} e^{-iqa} + cc.$$
(14)

Substituting eqs. (12)–(14) into eq. (10), the nonlinear dispersion relation of the nonlinear system be obtained by

$$\cosh(qL_1) = 1 - \frac{(1+\alpha)\Omega^2}{2} - \frac{\alpha^2 \Omega^4}{2(\beta - \alpha\Omega^2 + 2i\zeta_{\tau}\Omega + 3\beta\eta A_{1,i}\overline{A}_{1,i})}.$$
 (15)

Besides, the designed structure under out-of-plane motion is simplified (see Figure 4). Compared with the equivalent model of the in-plane motion, the equivalent model for the out-of-plane motion treats the connection (the flexible beam) between the resonator and the frame as a nonlinear spring with damping along the z-direction (k_z^{non} and c_z). Meanwhile, the shear stiffness between the adjacent frame is simulated by linear spring K_z . The equation of motion of the lumped mass and the resonator can be expressed as

$$\begin{cases}
M_0 \frac{d^2 z_j}{dt^2} + K_z (2z_j - z_{j-1} - z_{j+1}) + m_r \frac{d^2 w_j}{dt^2} = 0, \\
m_r \frac{d^2 w_j}{dt^2} + c_z \frac{dw_j}{dt} + F_z^{\text{non}} + m_r \frac{d^2 z_j}{dt^2} = 0,
\end{cases}$$
(16)

where z_j and w_j denote the displacements of the *j*th lumped mass and the local mass along the *z*-direction, respectively. The nonlinear restoring force F_z^{non} can refer to eq. (2).

Based on the Bloch theorem and harmonic balance method, the nonlinear dispersion relation of the equivalent model under out-of-plane motion can be derived. Since the solution process is similar to that of the in-plane dispersion relation, no more tautology here. Finally, the nonlinear dispersion relation of the equivalent model in out-of-plane motion is expressed as

$$\cosh(qL_1) = 1 - \frac{(1+\alpha)\Omega^2}{2} - \frac{\alpha^2 \Omega^4}{2(\gamma - \alpha \Omega^2 + 2i\zeta_z \Omega + 3b\gamma B_{1,i} \overline{B}_{1,i} / k_z)},$$
(17)

where the damping ratio $\zeta_z = c_z/(2\sqrt{MK_z})$ and the coefficient $\gamma = k_z/K_z$, $B_{k,j}$ is the time-domain amplitude of the *j*th resonator along the *z*-direction.

3.2 Experiment

The experimental layout is shown in Figure 5. The frame and the curved beam of the experimental samples are manufactured by 3D laser printing with epoxy. The main-slave resonators are made by wire cutting technology with steel material. The resonators are bonded in the flexible beam by the super glue. The machining precisions of the 3D laser printing and wire cutting technology are 0.02 and 0.01 mm, respectively.

The excitation signal is generated by the control device (DH8303) and transmitted to the shaker (SINOCERA JZK-5) through the power amplifier (SINOCERA YE5871A). The shaker delivers the excitation signal to the experimental samples, and the acceleration response is measured by the lightweight accelerometer (DH 1A339E). The acceleration signals are collected by the data acquisition system (DH8303). Finally, the transmission spectra can be calculated by the excitation signal (input signal) and the acceleration response (output signal).

4 Results and discussion

In this part, the dispersion curves calculated by the semianalytical method are verified by the finite element method. The effects of different mass configurations of main-slave resonators, support stiffness, and excitation amplitudes on dispersion relations and wave transmission characteristics are analyzed. The law of wave propagation is proved by experiment and numerical simulation in the finite periodic structure.

4.1 Dispersion relation under different parameters

The dispersion relation under a specific parameter set (see Tables 1 and 2) is given in Figure 6(a). The bandgaps for inplane and out-of-plane motions are in the range of 140.6-276.0 and 139.6-297.6 Hz, respectively. The real part $Re(qL_1)$ represents the change of phase and the imaginary part $Im(qL_1)$ denotes the rate of wave attenuation [59].

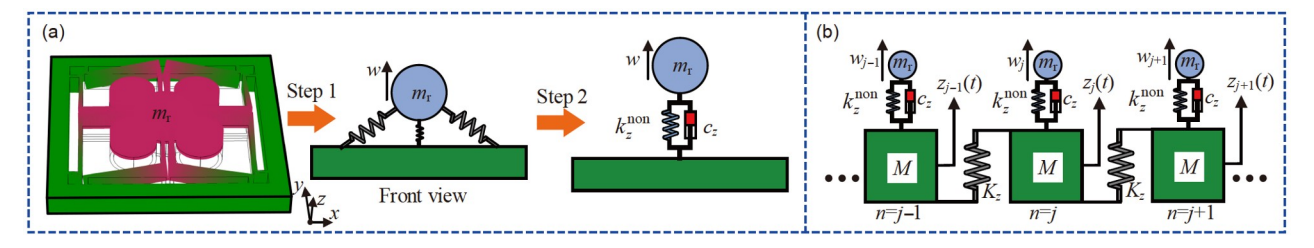


Figure 4 (Color online) Lumped mass-spring model for the out-of-plane motion. (a) Simplified process of the unit cell; (b) infinite periodic structure.

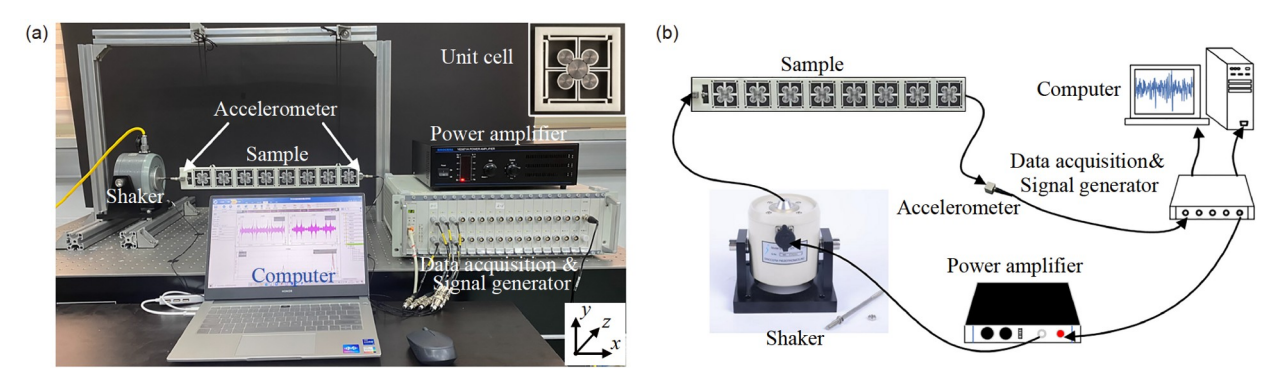


Figure 5 (Color online) Experiment. (a) Experimental setup; (b) flow chart of the vibration test.

Table 1 Geometric parameters

Parameters	Value	Parameters	Value
L_1 (mm)	60	R_1 (mm)	8
L_2 (mm)	50	R_2 (mm)	6
L_3 (mm)	20	δ (mm)	1
L_4 (mm)	4	h (mm)	5

Table 2 Material parameters

Materials	Frame/beams (epoxy)	Resonator (steel)
Young's modulus (GPa)	2.6	210
Density (kg/m ³)	1120	7800
Poisson's ratio	0.41	0.28

Within the bandgap, as the frequency increases, the absolute value of the imaginary part decreases, which implies a decline in the rate of wave attenuation. The analytical results are verified by the finite element simulations (see Figure 6(b)). The in-plane and out-of-plane dispersion curves by the semi-analytical method are similar to that of the finite element method. The eigenmodes of the unit cell at the IP1, IP2, OP1, and OP2 are shown in Figure 6(c) (the points IP1 and IP2 denote the beginning and ending frequencies of the in-plane bandgap; the points OP1 and OP2 denote the beginning and ending frequencies of the out-of-plane bandgap). For the eigenmodes at the beginning frequencies IP1 and OP1, the motion of the resonator dominates and the energy is mainly absorbed by the resonator. While at the ending frequencies IP2 and OP2, the motion of the frame dominates and the

frame acts like a rigid body [60].

The designed structure provides more possibilities for bandgap adjusting with mass, stiffness, and geometric nonlinearity. The material of the resonator is replaced with epoxy (see Table 2 for the material properties), and the new dispersion curves are shown in Figure 7(a). Compared with the results in Figure 6(a), the bandgap becomes higher, and the bandwidth becomes narrower. Different bandgap characteristics can be achieved through the mass arrangement of the main and slave resonators. When the length L_4 is changed to 16 mm (see Table 1 for other parameters), the new dispersion curves are shown in Figure 7(b). Compared with the results in Figure 6(a), with the increase of L_4 (the increase of beam stiffness), the in-plane and out-of-plane bandgaps move to a higher frequency range, and the bandwidth becomes wider. Besides, the influence of the nonlinear stiffness of the resonator on Im(qa) is analyzed in Figure 7(c). As the amplitude increases, the in-plane and out-of-plane bandgaps move to a higher frequency range, and the attenuation of the inplane wave gradually intensifies, while that of the out-ofplane wave slightly weakens.

4.2 Transmission characteristics

The wave transmission characteristic of a finite periodic structure (1×8 array, see Table 1 for structural parameters) is measured to verify the conclusion in Section 4.1. The experimental setup is shown in Figure 5, and the condition for in-plane and out-of-plane excitations are shown in Figure 8(a) and (b). The shaker exerts harmonic in-plane and out-of-plane

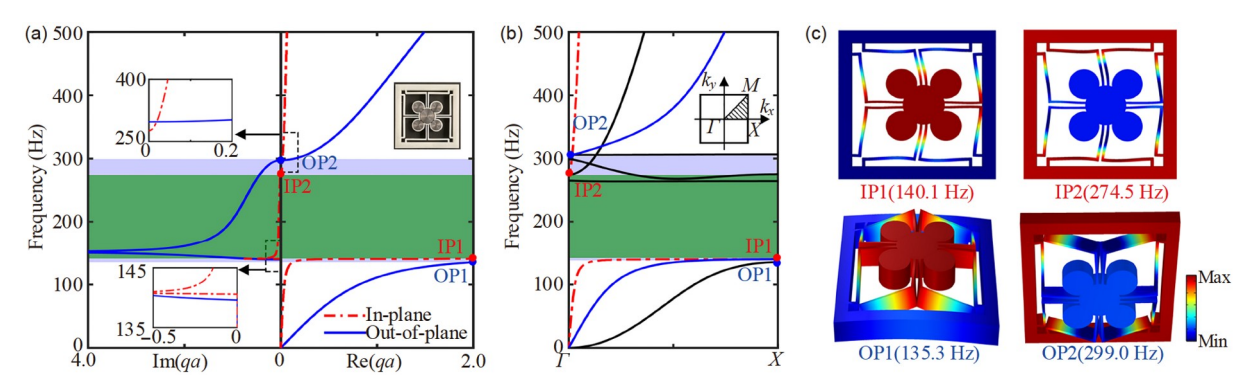


Figure 6 (Color online) Dispersion relation. (a) Analytical dispersion curves; (b) numerical dispersion curves by the finite element method; (c) eigenmodes at frequencies IP1, IP2, OP1, and OP2.

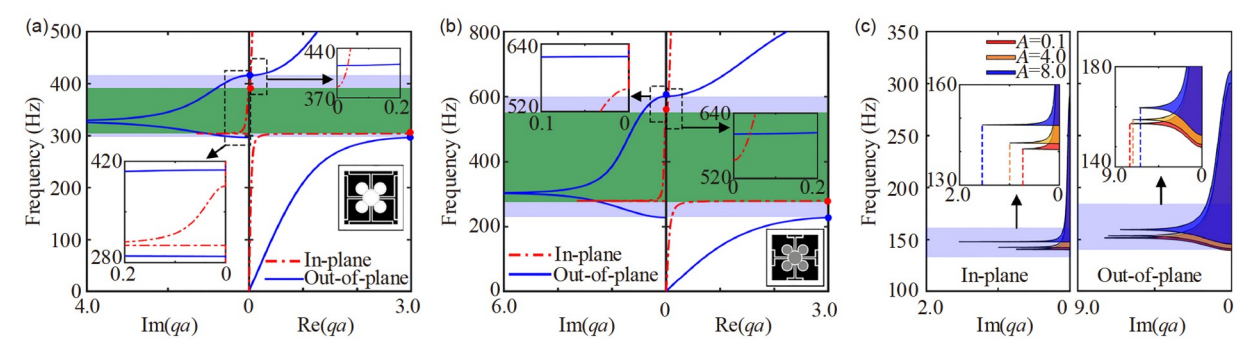


Figure 7 (Color online) Effects of the parameters on the dispersion curves. (a) Analytical dispersion curves with the resonator mass changed; (b) analytical dispersion curves with the supporting stiffness changed; (c) nonlinear dispersion curves under different amplitudes.

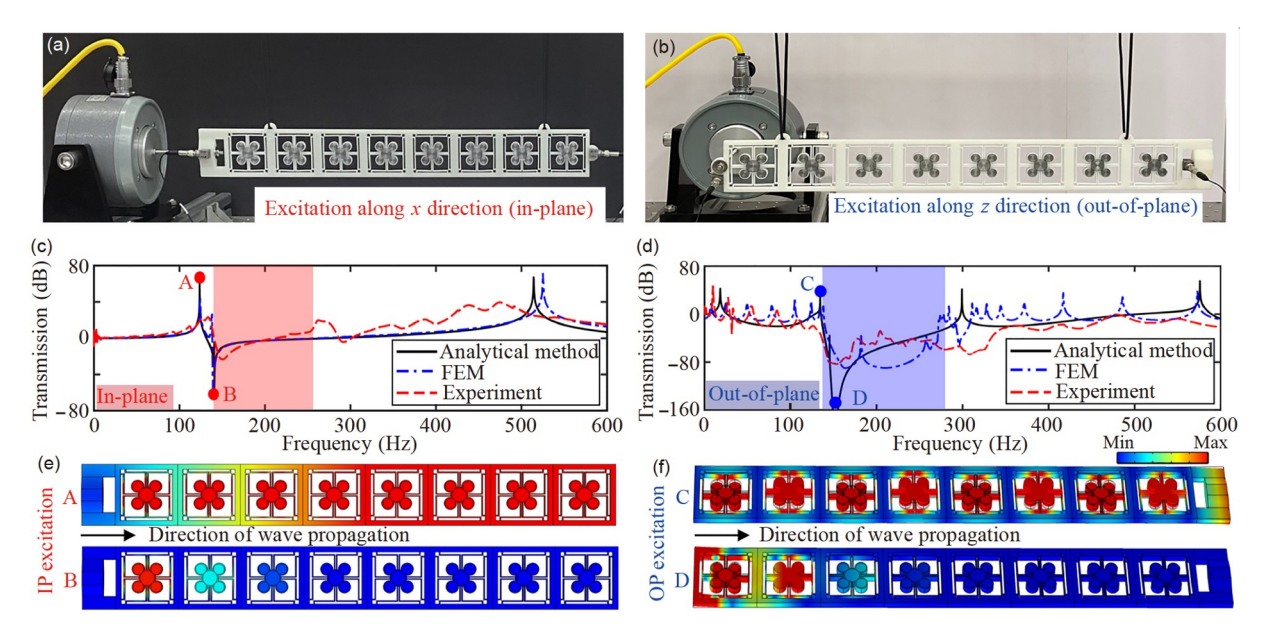


Figure 8 (Color online) Transmission characteristics for in-plane and out-of-plane motion. (a) Experiment under in-plane excitation; (b) experiment under out-of-plane excitation; (c) transmission spectra under in-plane excitation; (d) transmission spectra under out-of-plane excitation; (e) displacement fields at frequencies A and B; (f) displacement fields at frequencies C and D.

excitation on the sample, respectively. The transmissibility is defined as $T=20\log_{10}(A_{\rm out}/A_{\rm in})$. $A_{\rm out}$ and $A_{\rm in}$ are the acceleration amplitude of the output and input signals, respectively, which are collected by two accelerometers. The transmission

spectra obtained by the analytical method, finite element method and experiment are compared under in-plane and out-of-plane weak excitations (see Figure 8(c) and (d), the colored area is the theoretical bandgap). The displacement

fields at the excitation frequencies A (123.4 Hz), B (139.0 Hz), C (134.6 Hz), and D (151.6 Hz) are shown in Figure 8(e) and (f). According to the displacement field, the elastic wave can be attenuated by a finite number of unit cells within the bandgap (frequencies B and D), while at the resonance frequency outside the bandgap (frequencies A and C), the vibration amplitude at the output is amplified.

The nonlinear characteristics of the finite periodic structure are also verified by experimental transmission spectra under different excitation amplitudes (see Figure 9). The wave attenuation becomes enhanced with the increase of the in-plane excitation amplitude, and the bandgap shifts to the high-frequency range (see Figure 9(a)). As the out-of-plane excitation amplitude increases, the bandgap shifts to the high-frequency range, while the minimum in the transmission spectra does not change significantly (see Figure 9(b)). These conclusions coincide with those in Section 4.1. Due to the weak nonlinearity of the design structure [13,61], the influence of nonlinear excitation amplitude on the bandgap is limited. However, the geometric nonlinearity is also significant for bandgap regulation in a small range.

5 Applications

5.1 Waveguide path control

In this part, the control of the waveguide path with the mass arrangement of the main-slave resonators is achieved. Using the designed structure (L_4 =10 mm, see Table 1 for other parameters), the phase constant surfaces [62] under different resonator arrangements are calculated (see Figure 10). The main-slave resonators of cell A are all made of steel, and the resonators of cells B and C contain one and two slave resonators made of epoxy, respectively. The complete bandgap of cell A is 203.2–328.6 Hz. There is a rotational eigenstate with the frequency 267.1 Hz (the blue surface) in the bandgap, and its eigenstate is shown in Figure 10(a). When changing the material of the slave resonators (cells B and C). the complete bandgaps of cells B and C are shifted to the high-frequency range. The complete bandgaps of cells B and C are 215.9–341.6 and 236.6–350.6 Hz, respectively, and the eigenfrequencies of the rotational eigenstate are 302.3 and 335.0 Hz, respectively. It should be emphasized that the frame and the flexible beam of cells A, B, and C are the same, only the arrangements of the slave resonators are different. Next, the waveguide path control of the phononic crystal plate is realized by the mass arrangement of slave resonators.

For the waveguide path control, an 8×10 phononic crystal plate that is composed of cells A, B, and C is designed, and the low-reflecting boundary [63] is imposed on the edges of the plate (see the black box in Figure 11a). Path 1 is filled with cell A (cells in the red box), path 2 is filled with cell B (cells in the blue box), and the remaining part is filled with cell C. The bandgap of cell C is 236.6–350.6 Hz, and the eigenfrequencies of the rotational eigenstate of cells A and B

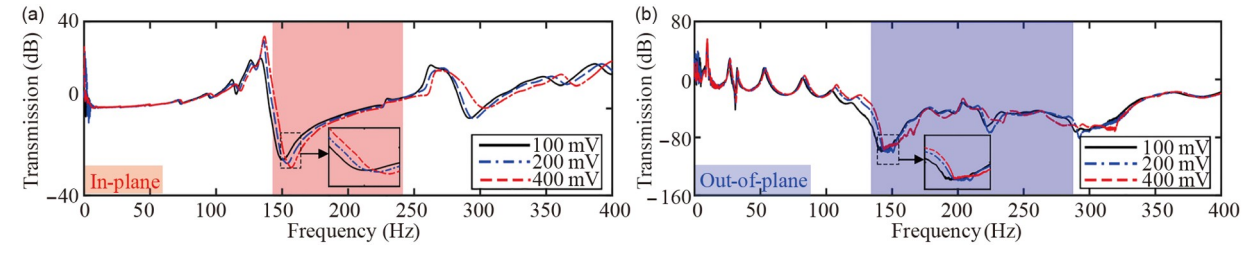


Figure 9 (Color online) Experimental transmission spectra under different excitation amplitudes. (a) In-plane excitation; (b) out-of-plane excitation.

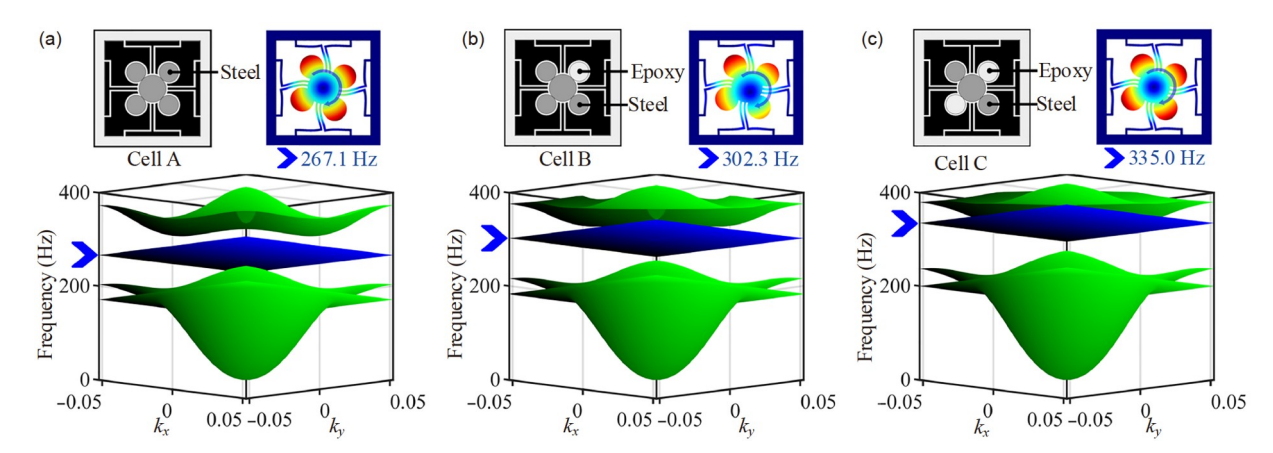


Figure 10 (Color online) Geometry and phase constant surfaces of the unit cell under different mass configurations. (a) Cell A; (b) cell B; (c) cell C.

(267.1, 302.3 Hz) are both within the bandgap of cell C. When the plate is excited by harmonic signals with frequencies 267.0 and 302.8 Hz, the rotational eigenstates of cells A and B will be excited, and the wave travel in paths 1 and 2, respectively. However, the waves with frequencies 267 and 302.8 Hz hardly propagate in cell C due to the excitation frequencies within the bandgap of cell C.

To verify the idea, the harmonic excitation (amplitude is 0.5 mm) along with the x- and y-direction is applied at the excitation point O (red star in Figure 11(a)). The amplitudefrequency responses of the points P and Q (green stars in Figure 11(a)) are extracted, as shown in Figure 11(b). The displacement field at frequencies 240 Hz (in bandgap), 267 Hz (path1), 302.8 Hz (path2), and 335 Hz (outside the bandgap) are plotted in Figure 11(c). It can be found that the wave can propagate along paths 1 and 2 at frequencies 267.0 and 302.8 Hz, respectively. This is because the specific excitation frequencies (267 and 302.8 Hz) excite the rotational eigenstates of cells A and B in paths 1 and 2, respectively. The wave with the frequency in the bandgap of cells A, B, and C (e.g., 240 Hz) is quickly attenuated in the phononic crystal plate. The wave with frequency outside the bandgap (e.g., 335 Hz) is difficult to control. The control of waveguide paths can be realized by using the different mass arrangements of main-slave resonators. Compared with the waveguide control of the topological insulator [63], an available idea for waveguide control is provided in this part.

5.2 Elastic wave imaging

Inspired by the acoustic imaging of the second-order topological insulators [53,54], the imaging of elastic waves in phononic crystal plates by the adjustment of main-slave resonators is achieved in this part. The geometrical parameters in Table 1 (L_4 =10 mm) are used to design the 5×4 phononic crystal plate (see Figure 12(a)). It should be noted that the phononic crystal plate in Figure 12(b) is composed of cells A and B in Section 5.1, and the phase constant surfaces of cells A and B refer to Figure 10. The mass arrangements of the main-slave resonators are shown in Figure 12(b) (green and blue are steel and epoxy, respectively). The harmonic excitation with frequency 267.0 Hz along x- and y-direction is applied at the excitation point (the red point in Figure 12(a)) and the low-reflecting boundary is imposed at the edge of the phononic crystal plate (see the black box in Figure 12(b)). The displacement fields under different resonator arrangements are shown in Figure 12(c).

Different imaging symbols (e.g., SJTU) can be realized

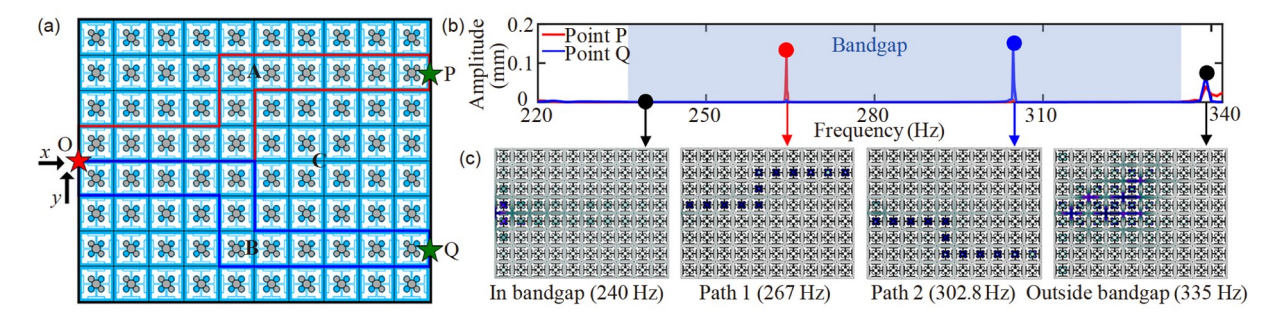


Figure 11 Application on the waveguide control. (a) Phononic crystal plate; (b) amplitude-frequency response; (c) displacement field.

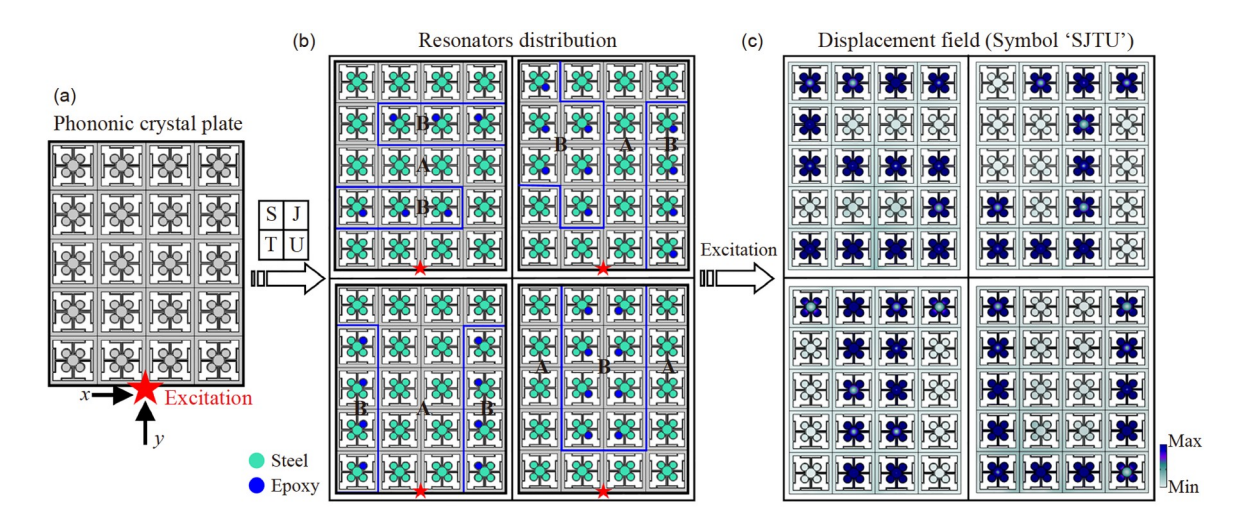


Figure 12 Application on the imaging of elastic waves. (a) Phononic crystal plate; (b) arrangement of the main-slave resonators; (c) displacement field for "SJTU".

under different arrangements of the main-slave resonators (see Figure 12(c)). When the excitation frequency is 267.0 Hz, the rotational eigenstate of cell A is excited. The wave can travel in cell A, while the wave can hardly propagate through cell B due to the excitation frequency (267 Hz) in its bandgap. Therefore, the symbols can be imaged along the path of cell A. Using the different arrangements of main-slave resonators, we can excite the same position of the phononic crystal plate but realize the elastic wave imaging along different paths.

5.3 Vibration isolation

A double-layered bolted plate is applied to demonstrate the application of the designed metamaterial in vibration isolation. The geometric schematic of the bolted plate is shown in Figure 13(a), and the parameters of the unit cell and plate are shown in Tables 1 and 3, respectively. The experimental sample is manufactured by 3D laser printing with epoxy and the double-layered plates are connected by 4×M5 steel bolts. The first layer is a metamaterial plate. The second layer is an ordinary plate without the metamaterial structure. The transmission characteristics of the double-layered bolted plate under in-plane and out-of-plane excitations are obtained by finite element method and experiments. The excitation positions of in-plane and out-of-plane are marked in the red and blue points of Figure 13(a), respectively. The experiment setup is shown in Figure 13(b). The transmission spectra obtained by the experiment and finite element method at the target location (green point) are plotted in Figure 13(c) and the displacement fields at frequencies D and F are shown in Figure 13(d). At frequencies D and F, the transmission of the target point on the second plate reaches the lowest under in-plane and out-of-plane excitations, respectively (see Figure 13(c)). It is because the in-plane and out-of-plane motions of the resonator are dominant at frequencies D and F (see Figure 13(d)). The vibration energy is

 Table 3
 Structure parameters of double-layered bolted metamaterial plate

Parameters	Value	Parameters	Value
$w_1(mm)$	60	w ₂ (mm)	30
w_3 (mm)	150	w ₄ (mm)	30
h_1 (mm)	7.5	h_2 (mm)	35
t (mm)	5	_	_

mainly absorbed by the resonators in the first layer, while little energy is transferred to the second layer.

Within the bandgap of the designed structure (the shaded regions denote the theoretical bandgaps), the vibration of the in-plane and out-of-plane can be effectively isolated. This is thanks to the energy absorption by the local resonators in the first metamaterial layer. This application could provide some inspiration for building metamaterials that are used to attenuate the seismic wave. The metamaterial plate is composed of finite cells, which have limited attenuation ability on elastic waves. It can be speculated that the attenuation ability of the metamaterial plate for in-plane and out-of-plane waves will be better when the number of the periodic unit cell layers increases. In engineering applications, the bandgap of the metamaterial should be designed to cover the resonant frequency band of the structure to reduce the damage by resonance.

6 Conclusions

In this study, a novel metamaterial with a two-dimensional bandgap is introduced. The broadband low-frequency bandgap of the metamaterial can be adjusted through the mass arrangement of the main-slave resonators, the flexible beam design, and the amplitude adjustment of the excitation. The proposed analytical method, finite element method, and experiment are used to analyze the bandgap characteristics of the designed structure. Some applications, waveguide

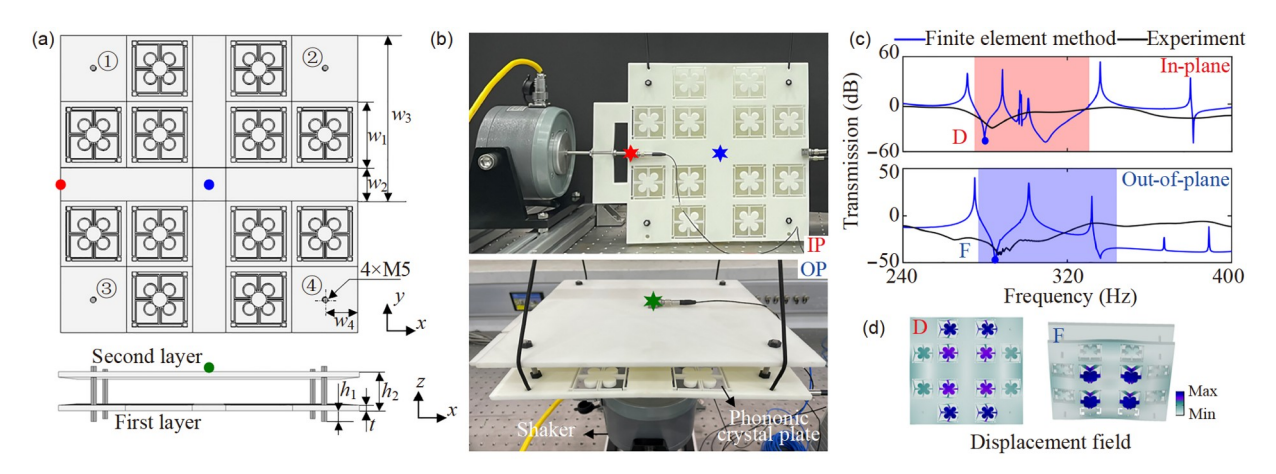


Figure 13 Application on the vibration isolation of the double-layer bolted plate. (a) Geometry; (b) experiment; (c) transmission spectra and the displacement field at frequencies D and F.

control, elastic wave imaging, and vibration isolation, are realized.

- (1) Effect of parameters on the bandgap: Arrangements of the main-slave resonators cause the shift of both in-plane and out-of-plane bandgaps. As the total mass of the resonator increases, the bandgap moves to the low-frequency range, and the bandwidth increases. The flexible beam induces geometric hardening nonlinearity. With the increase of the excitation amplitude, the in-plane and out-of-plane bandgaps move to the high-frequency range. In this case, the capacity of the metamaterial to attenuate elastic waves within the in-plane bandgap improves, while that within the out-of-plane bandgap decreases slightly.
- (2) Application of the designed metamaterial: By the arrangement of the main-slave resonators, the rotational eigenstates of the unit cell can shift through the bandgap. Under multi-directional excitations at the eigenfrequencies of the rotational eigenstates, the directional propagation of the waveguide is realized. The elastic wave imaging in phononic crystal plates is achieved based on a similar principle. We also used the metamaterial to isolate the vibration propagating through the double-layered bolted plates. The designed metamaterial can attenuate the in-plane and out-of-plane vibrations simultaneously, which has been verified by experiments and simulations. More engineering applications of this novel metamaterial can be expected.

This work was supported by the National Natural Science Foundation of China (Grant Nos. 11872243, 12272219, and 12121002).

Supporting Information

The supporting information is available online at tech.scichina.com and link.springer.com. The supporting materials are published as submitted, without typesetting or editing. The responsibility for scientific accuracy and content remains entirely with the authors.

- Surjadi J U, Gao L, Du H, et al. Mechanical metamaterials and their engineering applications. Adv Eng Mater, 2019, 21: 1800864
- 2 Ma F Y, Wang C, Liu C R, et al. Structural designs, principles, and applications of thin-walled membrane and plate-type acoustic/elastic metamaterials. J Appl Phys, 2021, 129: 231103
- 3 Dalela S, Balaji P S, Jena D P. A review on application of mechanical metamaterials for vibration control. Mech Adv Mater Struct, 2022, 29: 3237–3262
- 4 Li L, Zhang X, Song C, et al. Progress, challenges, and perspective on metasurfaces for ambient radio frequency energy harvesting. Appl Phys Lett, 2020, 116: 060501
- 5 Choi J, Jung I, Kang C Y. A brief review of sound energy harvesting. Nano Energy, 2019, 56: 169–183
- 6 Lee G, Lee D, Park J, et al. Piezoelectric energy harvesting using mechanical metamaterials and phononic crystals. Commun Phys, 2022, 5: 94
- 7 Chen Y, Liu X, Hu G. Latticed pentamode acoustic cloak. Sci Rep, 2015. 5: 15745
- 8 Yang R, Zhang X, Wang G. A hybrid acoustic cloaking based on binary splitting metasurfaces and near-zero-index metamaterials. Appl Phys Lett, 2022, 120: 021603
- 9 Jiang T, Li C, He Q, et al. Randomized resonant metamaterials for

- single-sensor identification of elastic vibrations. Nat Commun, 2020, 11: 2353
- Jiang T, He Q. Spatial information coding with artificially engineered structures for acoustic and elastic wave sensing. Front Phys, 2022, 10: 1024964
- 11 Fang D, Zhang Y. Mechanical metamaterials: Advanced designs and manufacture. Curr Opin Solid State Mater Sci, 2021, 25: 100934
- 12 Yuan X, Chen M, Yao Y, et al. Recent progress in the design and fabrication of multifunctional structures based on metamaterials. Curr Opin Solid State Mater Sci, 2021, 25: 100883
- 13 Fang X, Wen J, Bonello B, et al. Ultra-low and ultra-broad-band nonlinear acoustic metamaterials. Nat Commun, 2017, 8: 1288
- 14 Li H, Hu Y, Huang H, et al. Broadband low-frequency vibration attenuation in 3D printed composite meta-lattice sandwich structures. Compos Part B-Eng, 2021, 215: 108772
- 15 Wang Y F, Wang Y Z, Wu B, et al. Tunable and active phononic crystals and metamaterials. Appl Mech Rev, 2020, 72: 040801
- 16 Ma G, Sheng P. Acoustic metamaterials: From local resonances to broad horizons. Sci Adv, 2016, 2: 1501595–e1501595
- 17 Xi C, Dou L, Mi Y, et al. Inertial amplification induced band gaps in corrugated-core sandwich panels. Compos Struct, 2021, 267: 113918
- 18 Muhammad, Lim C W. Phononic metastructures with ultrawide low frequency three-dimensional bandgaps as broadband low frequency filter. Sci Rep, 2021, 11: 7137
- 19 Gao P, Climente A, Sánchez-Dehesa J, et al. Single-phase metamaterial plates for broadband vibration suppression at low frequencies. J Sound Vib, 2019, 444: 108–126
- 20 Chem B, Jiang Y, Liu C, et al. Dynamic behavior of soft, resonant metamaterials: Experiments and simulations. J Appl Phys, 2021, 129: 135104
- 21 Gao Y, Wang L. Nonlocal active metamaterial with feedback control for tunable bandgap and broadband nonreciprocity. Int J Mech Sci, 2022, 219: 107131
- 22 Wang K, Zhou J, Ouyang H, et al. A semi-active metamaterial beam with electromagnetic quasi-zero-stiffness resonators for ultralow-frequency band gap tuning. Int J Mech Sci, 2020, 176: 105548
- 23 Tan X, Chen S, Wang B, et al. Real-time tunable negative stiffness mechanical metamaterial. Extreme Mech Lett, 2020, 41: 100990
- 24 Pu H, Yuan S, Peng Y, et al. Multi-layer electromagnetic spring with tunable negative stiffness for semi-active vibration isolation. Mech Syst Signal Process, 2019, 121: 942–960
- 25 Chen Z, Sun S, Deng L, et al. Investigation of a new metamaterial magnetorheological elastomer isolator with tunable vibration bandgaps. Mech Syst Signal Process, 2022, 170: 108806
- 26 Zhu H F, Sun X W, Song T, et al. Tunable characteristics of low-frequency bandgaps in two-dimensional multivibrator phononic crystal plates under prestrain. Sci Rep, 2021, 11: 8389
- 27 Cai Y, Wu J H, Xu Y, et al. Realizing polarization band gaps and fluid-like elasticity by thin-plate elastic metamaterials. Compos Struct, 2021, 262: 113351
- 28 Yan Z, Xiao H, Liu Y, et al. Band-gap dynamics and programming for low-frequency broadband elastic metamaterial. Compos Struct, 2022, 291: 115535
- 29 An X, Fan H, Zhang C. Elastic wave and vibration bandgaps in planar square metamaterial-based lattice structures. J Sound Vib, 2020, 475: 115292
- 30 Li C, Jiang T, He Q, et al. Stiffness-mass-coding metamaterial with broadband tunability for low-frequency vibration isolation. J Sound Vib, 2020, 489: 115685
- 31 Muhammad, Lim C W, Li J T H, et al. Lightweight architected lattice phononic crystals with broadband and multiband vibration mitigation characteristics. Extreme Mech Lett, 2020, 41: 100994
- 32 Zhang H K, Feng X Q. Buckling-regulated bandgaps of soft metamaterials with chiral hierarchical microstructure. Extreme Mech Lett, 2021, 43: 101166
- 33 Yin X, Zhang S, Xu G K, et al. Bandgap characteristics of a tensegrity metamaterial chain with defects. Extreme Mech Lett, 2020, 36:

- 100668
- 34 Huang Y, Huang Y, Chen W, et al. Flexible manipulation of topologically protected waves in one-dimensional soft periodic plates. Int J Mech Sci, 2020, 170: 105348
- 35 Xiong Y, Xu A, Wen S, et al. Optimization of vibration band-gap characteristics of a periodic elastic metamaterial plate. Mech Adv Mater Struct, 2022, doi: 10.1080/15376494.2022.2070804
- 36 Xia Y, Ruzzene M, Erturk A. Dramatic bandwidth enhancement in nonlinear metastructures via bistable attachments. Appl Phys Lett, 2019, 114: 093501
- 37 Patil G U, Matlack K H. Review of exploiting nonlinearity in phononic materials to enable nonlinear wave responses. Acta Mech, 2022, 233: 1–46
- 38 Yu M, Fang X, Yu D. Combinational design of linear and nonlinear elastic metamaterials. Int J Mech Sci, 2021, 199: 106422
- 39 Jiang T, He Q. Dual-directionally tunable metamaterial for low-frequency vibration isolation. Appl Phys Lett, 2017, 110: 021907
- 40 Bilal O R, Hussein M I. Ultrawide phononic band gap for combined in-plane and out-of-plane waves. Phys Rev E, 2011, 84: 065701
- 41 Hu G, Austin A C M, Sorokin V, et al. Metamaterial beam with graded local resonators for broadband vibration suppression. Mech Syst Signal Process, 2021, 146: 106982
- 42 Wen J H, Wang G, Yu D L, et al. Study on the vibration band gap and vibration attenuation property of phononic crystals. Sci China Ser E-Tech Sci, 2008, 51: 85–99
- 43 Bao H, Wu C, Zheng W, et al. Vibration bandgap of a locally resonant beam considering horizontal springs. J Vib Control, 2021, 28: 452– 464
- 44 Fang X, Sheng P, Wen J, et al. A nonlinear metamaterial plate for suppressing vibration and sound radiation. Int J Mech Sci, 2022, 228: 107473
- 45 Zhao P, Zhang K, Qi L, et al. 3D chiral mechanical metamaterial for tailored band gap and manipulation of vibration isolation. Mech Syst Signal Process, 2022, 180: 109430
- 46 Zhang Q, Chen Y, Zhang K, et al. Programmable elastic valley Hall insulator with tunable interface propagation routes. Extreme Mech Lett, 2019, 28: 76–80
- 47 Zhao J F, Yuan W T, Bonello B, et al. Rainbow guiding of the lowest-order antisymmetric Lamb mode in phononic crystal plate. Sci China Tech Sci, 2019, 62: 458–463
- 48 Gao N, Qu S, Si L, et al. Broadband topological valley transport of

- elastic wave in reconfigurable phononic crystal plate. Appl Phys Lett, 2021. 118: 063502
- 49 Chen Z, Wang X, Lim C W, et al. Robust large-area elastic transverse wave transport in active acoustic metamaterials. J Appl Phys, 2022, 131: 185112
- 50 Lan C, Hu G, Tang L, et al. Energy localization and topological protection of a locally resonant topological metamaterial for robust vibration energy harvesting. J Appl Phys, 2021, 129: 184502
- 51 Zhang P, Biligetu P, Qi D X, et al. Mechanical design and energy absorption of 3D novel hybrid lattice metamaterials. Sci China Tech Sci, 2021, 64: 2220–2228
- 52 Liu Y, Xu Y, Zhang S C, et al. Model for topological phononics and phonon diode. Phys Rev B, 2017, 96: 064106
- 53 Zhang Z, Long H, Liu C, et al. Deep-subwavelength holey acoustic second-order topological insulators. Adv Mater, 2019, 31: 1904682
- 54 Ma F, Huang Z, Liu C, et al. Acoustic focusing and imaging via phononic crystal and acoustic metamaterials. J Appl Phys, 2022, 131: 011103
- 55 Dai H, Xia B, Yu D. Microparticles separation using acoustic topological insulators. Appl Phys Lett, 2021, 119: 111601
- 56 Dai H, Chen T, Jiao J, et al. Topological valley vortex manipulation of microparticles in phononic crystals. J Appl Phys, 2019, 126: 145101
- 57 Lazarov B S, Jensen J S. Low-frequency band gaps in chains with attached non-linear oscillators. Int J Non-Linear Mech, 2007, 42: 1186–1193
- 58 Brillouin L. Wave Propagation in Periodic Structures: Electric Filters and Crystal Lattices. New York: Dover Publications Inc., 2003
- 59 Wang K, Zhou J, Xu D, et al. Lower band gaps of longitudinal wave in a one-dimensional periodic rod by exploiting geometrical nonlinearity. Mech Syst Signal Process, 2019, 124: 664–678
- 60 Yao S, Zhou X, Hu G. Experimental study on negative effective mass in a 1D mass-spring system. New J Phys, 2008, 10: 043020
- 61 Fang X, Wen J, Bonello B, et al. Wave propagation in one-dimensional nonlinear acoustic metamaterials. New J Phys, 2017, 19: 053007
- 62 Wen J, Yu D, Cai L, et al. Acoustic directional radiation operating at the pass band frequency in two-dimensional phononic crystals. J Phys D-Appl Phys, 2009, 42: 115417
- 63 Zhang Q, Chen Y, Zhang K, et al. Dirac degeneracy and elastic topological valley modes induced by local resonant states. Phys Rev B, 2020, 101: 014101